

Polarization and local disorder effects on the properties of Er^{3+} -doped $\text{XBi}(\text{YO}_4)_2$, $\text{X}=\text{Li}$ or Na and $\text{Y}=\text{W}$ or Mo , crystalline tunable laser hosts

Mauricio Rico, Antonio Méndez-Blas, Vladimir Volkov, María Ángeles Monge, Concepción Cascales, and Carlos Zaldo

*Consejo Superior de Investigaciones Científicas, Instituto de Ciencia de Materiales de Madrid,
c/Sor Juana Inés de la Cruz 3, Madrid 28049, Spain*

Andreas Kling

*Instituto Tecnológico e Nuclear, Estrada Nacional No. 10. 2686-953 Sacavém and Centro de Física Nuclear
da Universidade de Lisboa, Avenida Prof. Gama Pinto 2, Lisbon 1649-003, Portugal*

María Teresa Fernández-Díaz

Institut Laue Langevin, ILL Boîte Postale 156X, Grenoble 38042, France

Received December 19, 2005; revised May 3, 2006; accepted May 16, 2006; posted June 2, 2006 (Doc. ID 66670)

APC:
#1

Pure and Er-doped ($[\text{Er}]_{\text{crystal}} \leq 2.4 \times 10^{20} \text{ cm}^{-3}$), $\text{NaBi}(\text{WO}_4)_2$ (NBW), $\text{NaBi}(\text{MoO}_4)_2$, and $\text{LiBi}(\text{MoO}_4)_2$ crystals have been grown by the Czochralski method. The three crystal hosts have similar structural and optical properties. The noncentrosymmetric space group $I\bar{4}$ (No. 82) crystallographic structure has been established through 300 K single-crystal x-ray and neutron (for NBW only) diffraction. Er^{3+} energy levels were determined experimentally and simulated in the S_4 symmetry through a crystal-field analysis. With this background, the large spectroscopic bandwidths observed were ascribed to the presence of two $2b$ and $2d$ sites for Er^{3+} and to different short-range Na^+ and Bi^{3+} distributions around both sites. The radiative properties of Er^{3+} are described by the Judd–Ofelt theory achieving branching ratios and radiative lifetimes for transitions useful as laser channels. The $^4I_{13/2} \rightarrow ^4I_{15/2}$ laser channel ($\lambda \approx 1.5 \mu\text{m}$) shows a peak emission cross-section σ_{EMI} ($\lambda \approx 1530 \text{ nm}$) $\approx 0.5 \times 10^{-20} \text{ cm}^2$, and a quantum efficiency $\eta \approx 0.68$ to 0.74 . The laser emission is envisaged to be tunable by $\Delta\lambda \approx 100 \text{ nm}$. © 2006 Optical Society of America

OCIS codes: 140.3500, 160.3380, 160.4760, 160.5690, 300.1030, 300.2140.

1. INTRODUCTION

Double tungstate (DT) and molybdate (DM) crystals with the chemical formula $\text{XT}(\text{YO}_4)_2$, where X is a monovalent cation, T is a trivalent one (often a trivalent rare earth), and $\text{Y}=\text{Mo}^{6+}$ or W^{6+} are crystalline hosts accepting a large concentration of laser active trivalent lanthanides. At temperatures close to their melting or decomposition points most of these compounds show the tetragonal crystalline structure of the scheelite, CaWO_4 , with the centrosymmetric space group (SG) $I4_1/a$ (No. 88). Upon cooling to RT, phase transitions (polymorphic transformations) to other crystalline structures with lower symmetry may occur.

DT and DM compounds with tetragonal crystalline structure are found at RT when no polymorphic transformation occurs upon cooling. In a limited number of cases, namely, $\text{NaT}(\text{WO}_4)_2$ ($\text{T}=\text{Bi}, \text{La}-\text{Er}$), $\text{NaBi}(\text{MoO}_4)_2$ (NBW), and $\text{KT}(\text{MoO}_4)_2$ ($\text{T}=\text{La}-\text{Nd}$), a congruent melting is also found, and therefore the efficient Czochralski (Cz) growth technique can be applied to obtain single crystals. In the tetragonal lattice, the monovalent X^+ and trivalent T^{3+} ions randomly share the same cationic sublattice. In

this case, a variety of crystal-field (CF) potentials on the sites occupied by T ions occur, and therefore the optical absorption (OA) and emission bands of optically active lanthanides are broad. The large bandwidths associated with the X/T disorder allow laser tunability in broad spectral ranges. In fact, about 40 nm range of tunability has been recently reported for the Yb^{3+} laser emission in $\text{NaGd}(\text{WO}_4)_2$ (Ref. 1), $\text{NaLa}(\text{WO}_4)_2$, and $\text{NaLa}(\text{MoO}_4)_2$ (Ref. 2). This broad emission band allowed sub-100 fs laser pulses in $\text{NaGd}(\text{WO}_4)_2$ by mode locking,³ and it promises even shorter (<50 fs) laser pulses by using pulse compression techniques.

These outstanding applications of disordered DT and DM crystals have been recognized only recently, and therefore the preparation and characterization of these “disordered” hosts are little developed. In particular, Li compounds have been very scarcely investigated. In the context of exploitation of crystals with large bandwidths, this work studies the crystal growth and the relationship of crystal structure with optical properties of $\text{LiBi}(\text{MoO}_4)_2$ (LBM), and its doping with Er^{3+} in comparison to the close-related NBW, and $\text{NaBi}(\text{MoO}_4)_2$ (NBM), crystals.

The efficiency of the NaBi-based DT and DM crystals as laser hosts was shown for Nd^{3+} (Ref. 4). Er^{3+} has several laser channels operating at RT. Of particular interest are the $1.5\ \mu\text{m}$ $^4I_{13/2} \rightarrow ^4I_{15/2}$ laser emission for long-distance fiber communications and the $2.9\ \mu\text{m}$ $^4I_{11/2} \rightarrow ^4I_{13/2}$ laser emission for medical applications, but other laser channels also involve all multiplets below $^4S_{3/2}$ (Ref. 4). Previous works reported some information of Er^{3+} emission spectroscopy in NBW^{5,6} but ignoring the polarized character of the transitions already known.⁷ Here, the Er^{3+} spectroscopy is discussed in terms of the host disorder with explicit consideration of its polarized character, and the perspectives for laser operation are investigated.

2. EXPERIMENTAL TECHNIQUES

Product synthesis and crystal growth experiences were made using Pt crucibles and a Si_2Mo heating element furnace. The temperature was set with a resolution of $\pm 0.2^\circ\text{C}$ using an Eurotherm 818P temperature controller.

The composition analyses of the hosts have been made by ion-beam techniques. Rutherford backscattering (RBS) measurements were performed using 1.8 MeV H^+ ions from a 3.1 MV van de Graaff accelerator at Sacavém. A surface barrier detector with a small solid angle (1.7 msr) located at 160° recorded the spectrum of the backscattered protons for the verification of the concentration of the crystal constituents other than Li. Moreover, the α particles produced in the nuclear reaction between protons and Li were detected by an annular surface barrier detector located at 180° with respect to the beam. The large solid angle (14 msr) allowed for the recording of α -particle spectra with sufficient statistics despite the low-reaction cross section and atomic concentration of Li in the sample.

The Er concentration in the crystals was determined by inductively coupled plasma (ICP) analyses conducted on a Thermo Jarrel As IRIS Advantage axial plasma spectrometer. For the Er analysis, the spectral line at $\lambda = 337.271\ \text{nm}$ was selected, and the signal background was established and discounted. For each crystal host, only the most concentrated sample was analyzed by ICP; the Er concentration for other crystals was calculated by

the comparison of their integrated OA. Table 1 summarizes the Er concentrations in the crystals used.

X-ray diffraction (XRD) analyses of pure NBW, NBM, and LBM as well as Er-doped NBW crystals have been performed from data collected at RT by a Siemens SMART CCD diffractometer equipped with a normal focus 3 kW sealed tube. Small prismatic single crystals cut from each grown material were selected in order to reduce the possibility of twinning and to minimize the absorption effect. Data were collected over a quadrant of the reciprocal space by a combination of three sets of exposures. Each set had a different φ angle for the crystal, and each exposure of 20 s covered 0.3° in ω . The crystal-to-detector distance was 5.08 cm. For each crystal, unit cell parameters were determined by a least-squares fit of about 35 reflections with $I > 20\sigma(I)$. Further details are described later (see Table 3). Neutral-atom scattering factors for all atoms were used, and anomalous dispersion corrections were applied.⁸ All calculations were performed using the SHELXTL program,⁹ and ATOMS software for the structure plots. Also, scan intensity measurements of some selected individual hkl reflections have been performed at RT on an Enraf-Nonius CAD4 diffractometer, with Mo-K_α radiation.

Very precise and accurate measurements of Bragg intensities for a considerably more larger, $\sim 80\ \text{mm}^3$ crystal of NBW were also performed in the hot neutron four-circle diffractometer D9, at the Institut Laue Langevin (ILL), Grenoble, France. The monochromator is a Cu crystal in transmission geometry using the (220) planes. The used wavelength was $0.84\ \text{\AA}$ and the data collection required 4 days. Further details concerning the geometry, detector, and possible environments for the sample in the D9 equipment can be consulted at the ILL web page (www.ill.fr). Specific details of the current experiment are also described later (see Table 3).

For optical measurements, the crystals were oriented by using Laue XRD patterns, cut, and polished with diamond paste. Refractive indices were measured at 300 K by the minimum-deviation-angle method using prisms; the estimated error is ± 0.002 . OA measurements were made in a Varian spectrophotometer model Cary 5E ($\lambda = 200$ to $3000\ \text{nm}$). The sample temperature was varied in the 10–300 K range by using a He closed-cycle Oxford cryostat equipped with the proper temperature controller. For polarized measurements, the sample was inserted between a Glan–Taylor polarizer and a depolarizer sheet. The spectra are labeled as $\sigma(\mathbf{E} \perp c, \mathbf{H} \parallel c)$ or $\pi(\mathbf{E} \parallel c, \mathbf{H} \perp c)$; \mathbf{E} and \mathbf{H} are the electric and magnetic field components of the light, respectively. Photoluminescence (PL) was excited in the continuous mode with a Ti-sapphire laser, dispersed in a SPEX spectrometer ($f = 34\ \text{cm}$) and measured with a 77 K cooled Ge photodiode or a cooled Hamamatsu R928 photomultiplier. Lifetime measurements of $^4S_{3/2}$ level were excited with a dye laser (LSI, model DUO-220) using Couramin-540A. For the lifetime of the $^4I_{13/2}$ multiplet, we excited the $^4I_{11/2}$ multiplet at $\lambda \approx 980\ \text{nm}$ with a chopped Ti:sapphire laser and the emission at $\lambda = 1550\ \text{nm}$ was measured by a 77 K cooled Hamamatsu R5509-72 photodetector with 3 ns of rise time. In both cases, the signal was stored and averaged by a 500 MHz Tektronix TDS520 digital oscilloscope.

Table 1. Er Concentration and Segregation Coefficient, S , of the Crystals Used in This Work

Crystal	Er_{melt} mol. %	$\text{Er}_{\text{crystal}}$ mol. %	S	$\text{Er}_{\text{crystal}}$ $\times 10^{20}\ \text{cm}^{-3}$
NBW: Er^{3+}	0.02	0.03	1.5	0.02
	0.44	1.47	3.3	0.92
	0.88	3.85	4.3	2.41
NBM: Er^{3+}	0.16	1.2	7.5	0.75
	0.33	1.68	5.1	1.05
	0.73	3.45	4.7	2.15
LBM: Er^{3+}	0.03	0.11	3.7	0.07
	0.16	0.88	5.5	0.56
	0.3	1.22	4.0	0.78

3. EXPERIMENTAL RESULTS

A. Crystal Growth

Table 1 shows the Er-doped crystals used in this work. The crystal growth details of NBW and NBM have been offered in a previous work.¹⁰ The LBM phase was synthesized using Li_2CO_3 , Bi_2O_3 , and MoO_3 initial products and procedures similar to those described for NBM.¹⁰ The DTA of LBM showed a congruent melting at 650°C . Undoped and Er-doped crystals were pulled from the melt at a rate of $1.8\text{--}2.8\text{ mm/h}$ using undoped LBM seeds. The rotation speed was $4\text{--}6\text{ rpm}$, and the melt was allowed to cool during the growth process at a rate of $dT/dt = 0\text{--}0.4^\circ\text{C/h}$. Undoped LBM crystals show a yellow color associated with an absorption edge in the blue. Figure 1 shows a LBM crystal achieved and a transparent polished plate of NBW. Er segregation coefficients $S = [\text{Er}]_{\text{crystal}}/[\text{Er}]_{\text{melt}} > 1$ are found under all growth conditions for the considered Bi-based DT and DM (see Table 1).

B. Compositional Analysis

While the host composition of $\text{NaBi}(\text{YO}_4)_2$, $Y = \text{W}$ or Mo , crystals are well established in the previous work,¹⁰ the LBM composition must be assessed particularly for the light Li ion.

Figure 2(a) shows the RBS spectra of a LBM crystal. RBS is a very sensitive method to determine the concentration of elements with medium and large atomic numbers ($Z > 8$) in a sample, and thus the results of Fig. 2(a) provide reliable $\text{Bi}/\text{Mo} = 2$ and $\text{O}/\text{Mo} = 4$ molar ratios, considering that the elastic scattering for 1.8 MeV incident protons is about 3.2 times larger than the RBS cross section.¹¹ However, RBS fails in the detection of Li, and nuclear-reaction analysis (NRA) has to be used as an alternative ion-beam method. The ${}^7\text{Li}(p, \alpha){}^4\text{He}$ reaction¹² offers, owing to the high abundance of ${}^7\text{Li}$ (92.5%) in natural Li, a convenient way for detection, and it has therefore already been frequently applied.^{13,14}

This reaction has a high positive Q value ($Q = +17.4\text{ MeV}$) yielding two α particles, each with an energy of approximately 7.6 MeV for the reaction with

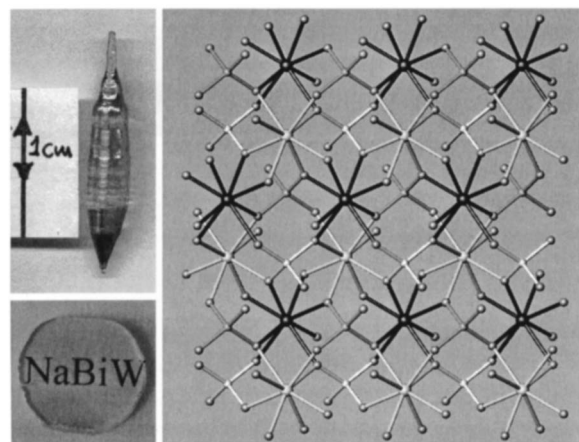


Fig. 1. (a) As-grown Er-doped LBM crystal boule. (b) Polished NBW plate grown by the CZ method. (c) ac view of the $X/\text{BiO}_8\text{--YO}_4$ coordinations containing dimeric $(X/\text{Bi})_2\text{O}_{14}$ units along the c axis (vertical direction).

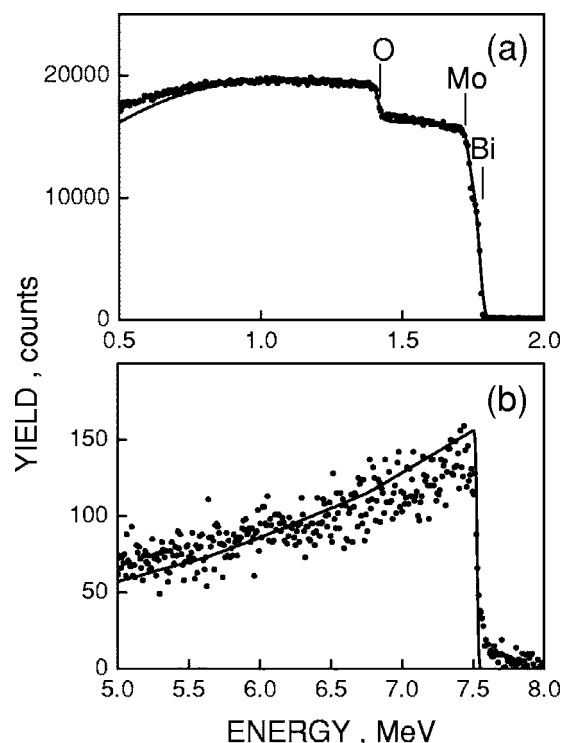


Fig. 2. (a) RBS spectrum and (b) NRA spectrum of an undoped LBM single-crystal. Points are the experimental results and the curves are the fits using the SENRAS simulation code.

1.8 MeV protons. The high energy of the released α particles enables the study of the Li content in the material without any overlapping RBS signals from any of the other constituents up to $8\text{ }\mu\text{m}$ depth. Figure 2(b) shows the α -particle spectra recorded for the LBM crystal together with a simulation performed using the SENRAS code.¹⁵ A best fit to the spectrum has been obtained for a ${}^7\text{Li}:\text{Bi}$ ratio of 0.89 that, taking into account the ${}^7\text{Li}$ natural abundance of 92.5%, provides a molar $\text{Li}:\text{Bi}$ ratio of 0.96 ± 0.08 in the crystal.

C. Crystalline Structure

NBW and NBM were initially ascribed to the SG $I4_1/a$ (No. 88).¹⁶ Later studies described these crystals in the noncentrosymmetric SG $I\bar{4}$ (No. 82) because of the presence of nonnegligible $(006, 00\bar{6}, 002, \bar{1}10, \text{ and } 1\bar{1}0)$ x-ray reflections.¹⁷ Recently the same authors have examined the RT crystalline structure of Cz-grown NBW (Ref. 18) and NBM crystals grown by the Stöber method.¹⁹ At that time, they did not find the aforementioned $00l$ and $h\bar{h}0$ reflections; therefore, they concluded that the correct symmetry was $I4_1/a$ instead of $I\bar{4}$. Moreover, it was found that NBM undergoes, at $T = 241\text{ K}$, a phase transition to the monoclinic SG $I2/a$ (No. 15). Although independent composition analyses of all these crystals were not provided, previous $I\bar{4}$ assignments have been attributed to a possible departure of the crystal composition stoichiometry.¹⁸ The crystalline structure of LBM was also ascribed to the symmetry of the SG $I4_1/a$ (Ref. 20), and a later work¹⁶ also assumes this SG.

Whichever of the two indicated tetragonal symmetries is the correct one for the $\text{XBi}(\text{YO}_4)_2$ hosts, they are struc-

turally disordered crystals owing to the distribution of the alkaline X^+ (Li or Na) and Bi^{3+} cations either at the unique $4b$ crystallographic site, with S_4 symmetry, when the material is described in the SG $I4_1/a$, or in the two independent $2b$ and $2d$ point sites, also S_4 , for crystals described in the SG $I\bar{4}$. In the latter case, although in both sites Bi^{3+} is coordinated to eight oxygens, owing to the loss of symmetry the Bi–O distances and bond angles are obviously different in each BiO_8 polyhedra. The inhomogeneous broadening observed at low temperature for optical bandwidths of Er^{3+} embedded in $XBi(YO_4)_2$ has its origin in the multiple local environments around Er^{3+} in the host, with small site-to-site CF differences. However, the magnitude of the broadening will be obviously related to the envisaged number of crystal sites for Er^{3+} , and a priori is expected to enlarge with increasing number of Er sites. Therefore ascertaining the crystalline structure is relevant for the correct interpretation of the observed Er^{3+} optical bandwidths.

The structural determination procedure used here consisted of an initial evaluation of the significance of some hkl reflections, which are systematic absences in SG $I4_1/a$, through their individual psi-scan intensity measurements. The reflections selected for this purpose were those constituting violations of the a plane, $h\bar{h}0$, $h \neq 2n$, and hence the SG $I4_1$ would be still possible, as well as those forbidden for the 4_1 axis, $00l$, l even but $l \neq 4n$, which leads to the SG $I\bar{4}$. After collecting each reflection several times, for every crystal, the average value is compared to the estimated background (EB) intensity obtained averaging $00l$ reflections, $l \neq 2n$, forbidden in all these SGs. It can be observed in Table 2 that the intensity of these reflections, and especially 002 and $1\bar{1}0$ are well above the EB level for the three matrices, NBW, NBM, and LBM, considered here.

Second, the analysis of single-crystal x-ray data for each pure host and for Er-NBW and the refinement of the crystal structure, that is, the determination of atomic coordinates, occupancy factors (OF) for shared cationic positions, $2d(I)$ and $2b(II)$, and thermal anisotropic displacements for all atoms, have also allowed for the presence of a certain number of systematic absence exceptions to be determined, for the a plane and for the 4_1 axis, with intensity $I > 3\sigma(F)$, that is, well above the $I > 2\sigma(F)$ threshold for reflections considered in the refinement, which undoubtedly indicated the noncentrosymmetric SG $I\bar{4}$. Furthermore, besides the assessment of the distortion

from the $I4_1/a$ to the $I\bar{4}$ symmetry, the crystal structure refinements also provide precise estimations of the X/Bi distribution over the sites $2d(I)$ and $2b(II)$ that they are sharing in each studied disordered crystal, which moreover lead to positive values of the anisotropic thermal displacement for all atoms and adequately low R_1 discrepancy factors. All these results are included in Table 3. More precise results have been obtained for the NBW refinement from single-crystal D9 neutron data, also shown in Table 3, and concerning the occupancy factors, they have turned out to be exactly the same whatever the origin of the diffraction data. Table 4 provides the derived main interionic distances in the crystals, which for NBW are the more precise, corresponding to neutron diffraction results.

It is worth noting that a slight alkali deficiency derived from the current x-ray analysis is observed for the LBM crystal, which confirmed NRA values shown previously. On the other hand, the LBM crystal appears as the crystal with lowest distortion from the centrosymmetric SG $I4_1/a$, i.e., the lowest number of observed reflections corresponding to systematic absences of $I4_1/a$ and cationic OF closer to random 0.5–0.5 values. The other crystals present larger departures from this situation, and the Er incorporation develops a more intense $I\bar{4}$ character, that is, more observed reflections not allowed in $I4_1/a$ and a higher degree of local cationic ordering derived of the different X/Bi OFs.

Figure 1 shows an ac projection of the $I\bar{4}$ crystal structure showing the alternated $2b$ and $2d$ positions for the X/Bi and the tetrahedral YO_4 groups.

D. Optical Characterization

1. Crystal Birefringence

As expected for a birefringent crystal, the OA of LBM in the blue region is anisotropic. The OA thresholds observed at 300 K are approximately 416 nm for π -polarized light and approximately 427 nm for σ -polarized light. Similar anisotropy in the UV optical absorption edges have been previously observed in NBW and NBM hosts.¹⁰

On the basis of the tetragonal unit cell determined from the XRD analysis in Subsection 3.C, the ordinary (n_o , $\perp c$ axis) and extraordinary (n_e , $\parallel c$ axis) refractive indices of LBM were determined. Figure 3 shows the results obtained and the Sellmeier coefficients achieved for a minimum least-squares deviation fitting the following formula:

$$n^2 = A + \frac{B}{1 - (C/\lambda)^2} - D\lambda^2. \quad (1)$$

Similar results for $NaBi(YO_4)_2$, $Y=W$ and Mo , have been already reported by us.¹⁰ It is interesting to note that the three Bi-based single-crystal hosts examined by us, namely, the NBW, NBM, and LBM, are negative uniaxial crystals with refractive index and birefringence ($\Delta n = |n_o - n_e|$) increasing from NBW to NBM and to LBM. Therefore LBM appears to be a promising material for optical waveguide fabrication on NBW or NBM substrates. In fact, the lattice mismatches for the

Table 2. Assessment of the $I4_1/a \rightarrow I\bar{4}$ Distortion from Individual Scan Intensity Measurements I_{hkl} versus Background Intensity EB

hkl X-Ray Reflections Forbidden in $I4_1/a$	NBW	NBM	LBM
$00l$, l even and $\neq 4n$:			
$1002/EB$	34/12	42/5	28/9
$1006/EB$	19/12	5/5	10/9
$h\bar{h}0$, $h \neq 2n$:			
$11\bar{1}0/EB$	25/12	25/5	15/9
$13\bar{3}0/EB$	15/12	7/5	14/9

Table 3. Crystal Data at 296(2) K and Structure Refinement Details of $X\text{Bi}(\text{YO}_4)_2$, $X=\text{Li}, \text{Na}$ $Y=\text{Mo}, \text{W}$, and Er-doped NBW
($[\text{Er}]_{\text{crystal}}=2.4 \times 10^{20} \text{ cm}^{-3}$)

Nominal formula	Ions				NBW ^{a-e,i}				NBW, Er ^{a,c,e,i}				NBM, Er ^{a,c,e,i}				NBM, Er ^{a,c,e,i}			
Unit cell dimensions (Å)					<i>a</i> = <i>b</i> = 5.2752(6)				<i>a</i> = <i>b</i> = 5.2827(7)				<i>a</i> = <i>b</i> = 5.2676(10)				<i>a</i> = <i>b</i> = 5.2178(8)			
					<i>c</i> = 11.503(2)				<i>c</i> = 11.514(2)				<i>c</i> = 11.552(12)				<i>c</i> = 11.469(2)			
Volume (Å ³)					320.11(9)				321.32(9)				320.54(12)				312.25(9)			
Calculated density (Mg/m ³)					7.549				7.521				5.718				5.699			
Absorption coefficient (mm ³)					63.338				63.100				31.307				32.066			
<i>F</i> (000)					612				612				484				468			
					137 ^j															
Crystal size (cm ³)					0.09 × 0.07 × 0.07				0.08 × 0.10 × 0.12				0.05 × 0.08 × 0.12				0.05 × 0.07 × 0.10			
					4 × 4 × 5															
θ range for data collection (°)					3.54 to 26.40				3.54 to 28.81				3.53 to 28.36				3.55 to 28.15			
					4.19 to 54.39															
<i>hkl</i> Limiting indices					−3 to 6, −6 to 1, −14 to 14				−6 to 6, −4 to 7, −8 to 15				−6 to 2, −6 to 6, −10 to 11				−6 to 6, −3 to 5, −15 to 8			
					−10 to 10, −10 to 10, −22 to 8															
Reflections collected/unique					671/314 [<i>R</i> (int) = 0.0414]				783/371 [<i>R</i> (int) = 0.0339]				704/268 [<i>R</i> (int) = 0.0397]				872/350 [<i>R</i> (int) = 0.0373]			
					1806 / 901 [<i>R</i> (int) = 0.0235]															
Data/restraints/parameters					314/0/30				371/0/30				268/0/30				350/0/30			
					901/2/32															
Goodness of fit on <i>F</i> ²					1.06				0.889				1.095				1.176			
Final <i>R</i> indices [<i>I</i> > 2σ(<i>I</i>)]					<i>R</i> ₁ = 0.1009, <i>wR</i> ₂ = 0.2443				<i>R</i> ₁ = 0.0488, <i>wR</i> ₂ = 0.1583				<i>R</i> ₁ = 0.0839, <i>wR</i> ₂ = 0.2229				<i>R</i> ₁ = 0.0389, <i>wR</i> ₂ = 0.1143			
					<i>R</i> ₁ = 0.0397, <i>wR</i> ₂ = 0.0783															
<i>R</i> indices (all data)					<i>R</i> ₁ = 0.1070, <i>wR</i> ₂ = 0.2515				<i>R</i> ₁ = 0.0579, <i>wR</i> ₂ = 0.1723				<i>R</i> ₁ = 0.0867, <i>wR</i> ₂ = 0.2283				<i>R</i> ₁ = 0.0481, <i>wR</i> ₂ = 0.1211			
					<i>R</i> ₁ = 0.0756, <i>wR</i> ₂ = 0.0795															
Extinction coefficient					0.06(3)				0.035(8)				0.13(3)				0.141(12)			
Atom, site, <i>x</i> , <i>y</i> , <i>z</i> , <i>U</i> (eq ^g)	X(1)/Bi(I)	2 <i>d</i>	1/2	0	1/4	13(6)	1/2	0	1/4	29(2)	1/2	0	1/4	10(3)	1/2	0	1/4	16(1)		
	X(2)/Bi(II)	2 <i>b</i>	1/2	1/2	0	8(7)	1/2	1/2	0	5(4)	1/2	1/2	0	8(2)	1/2	1/2	0	17(1)		
	Y(1)	2 <i>a</i>	0	0	0	5(3)	0	0	0	17(2)	0	0	0	4(2)	0	0	0	12(1)		
	Y(2)	2 <i>c</i>	0	1/2	1/4	6(5)	0	1/2	1/4	10(2)	0	1/2	1/4	2(2)	0	1/2	1/4	10(1)		
	O(1)	8 _g ^f	2420(40)	5840(40)	530(20)	14(6)	2420(30)	8480(30)	860(15)	23(4)	2410(30)	8500(30)	820(15)	12(5)	2406(15)	0.8496(1)	838(7)	23(2)		
			2411(10)	8483(8)	831(4)	17(1)										(5)				
	O(2)	8 _g ^f	2390(40)	3490(40)	1650(20)	18(17)	2350(30)	3510(30)	1663(16)	28(4)	2380(30)	3530(30)	1635(19)	10(5)	2414(15)	3481(15)	1660(7)	23(2)		
			2384(6)	3440(6)	1637(4)	14(1)														
Or ^h	X(I)/Bi(I)	2 <i>d</i>	0.35(2)/0.65(2)				0.34(2)/0.66(2)				0.55(1)/0.45(1)				0.480(5)/0.520(5)					
			0.37(2) / 0.63(2)																	
	X(II)/Bi(II)	2 <i>b</i>	0.54(3)/0.46(3)				0.58(2)/0.42(2)				0.47(1)/0.53(1)				0.492(5)/0.508(5)					
			0.54(3) / 0.46(3)																	
Systematic absence exceptions:																				
<i>hklI</i> > 3σ for 4 ₁ axis (Total <i>I</i> > 2σ)																				
2(4)																				
4(6)																				
3(3)																				
2(8)																				
<i>hklI</i> > 3σ for <i>a</i> place (Total <i>I</i> > 2σ)																				
1(13)																				
7(22)																				
9(22)																				
0(11)																				

^aXRD wavelength 0.71073 (Å).

^bNegative differential conductivity (ND) wavelength 0.84 (Å).

^cXRD absorption correction SADABS.

^dND absorption correction DATAP.

^eRefinement method: full matrix least squares on F^2 .

^fAtomic coordinates $\times 10^4$.

^g $U_{(\text{eq})}$ is defined as one third of the trace of the orthogonalized U_{ij} tensor.

^hOccupancy factor for the indicated site. They were refined with no restrains between $2b$ and $2d$ sites.

ⁱPositive anisotropic thermal displacements for all atoms have been obtained and are available from the authors.

^jItalics indicate results from neutron D9-ILL, Grenoble data.

LBM/NaBi(W or MoO₄)₂, $(\alpha_{\text{LBM}} - \alpha_{\text{sub}})/\alpha_{\text{sub}} = 1.04 \times 10^{-2}$ and 0.89×10^{-2} , respectively, are small and therefore low interfacial stress is expected. LBM layers can be grown by liquid phase epitaxy, as the melting point of LBM (650 °C) is lower than the melting points of NBW (935 °C) and NBM (871 °C). It is also interesting to note that the birefringence ($\Delta n \approx 0.1$) of these three Bi-based crystals is much larger than those found in lanthanide-based tetragonal DT crystals, such as NaLa(WO₄)₂ and NaGd(WO₄)₂ ($\Delta n < 0.005$).²¹

2. Er³⁺ Energy Levels

The analysis of the observed energy levels of Er³⁺ in NBW and NBM crystals and the parameterization of their CF effects have been studied by some of us in a previous work.⁷ The analysis is extended now to the LBM host.

The energy level Stark sequence of the fundamental ⁴I_{15/2} multiplet was determined from the polarized ⁴I_{13/2} emission shown in Fig. 4. These spectra were obtained after excitation in the ⁴F_{7/2} ($\lambda_{\text{exc}} = 488$ nm) multiplet and the emission $\lambda_{\text{EMI}} \approx 1.5$ μm has been referred to $E = 0$ cm⁻¹ for the largest wavelength peak observed. The Stark levels of multiplets ranging from ⁴I_{13/2} to ²H_{9/2} have been determined directly from the ground-state optical absorption (GSA) at 10 K. These latter spectra show some *hot bands* with small intensity due to the thermal population of the two first excited ⁴I_{15/2} Stark levels with energy < 40 cm⁻¹. Transitions from the fundamental ⁴I_{15/2}(0) Stark level are labeled with arrows in Fig. 4.

Table 4. Selected Bond Lengths (Å) for Pure NBW, NBM, and LBM and Doped Er-NBW Crystals^a

Ligands	NBW ^b	NBW: Er	NBM	LBM
Bi(I)/X(I)-O(1) × 4	2.489(4)	2.463(16)	2.50(2)	2.459(8)
Bi(I)/X(I)-O(2) × 4	2.487(3)	2.514(16)	2.523(16)	2.466(8)
Bi(II)/X(II)-O(1) × 4	2.481(3)	2.491(13)	2.478(17)	2.466(8)
Bi(II)/X(II)-O(2) × 4	2.475(4)	2.500(17)	2.47(2)	2.465(7)
Y(1)-O(1) × 4	1.781(4)	1.807(14)	1.768(17)	1.765(8)
Y(2)-O(2) × 4	1.801(4)	1.758(18)	1.779(16)	1.773(8)

^aX=Na or Li.

^bDistances corresponding to results from the neutron diffraction refinement.

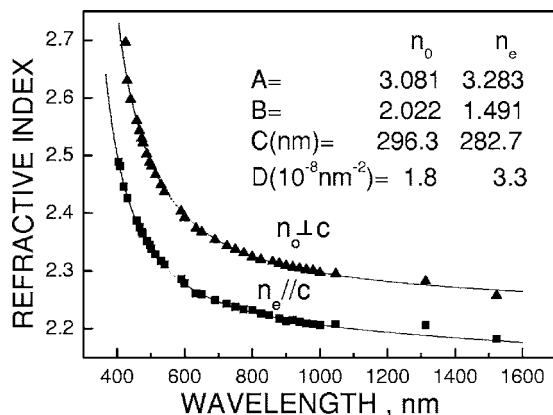


Fig. 3. Refractive index of 300 K dispersion of uniaxial LBM single crystal. The points are the experimental results and the curves the Sellmeier fits.

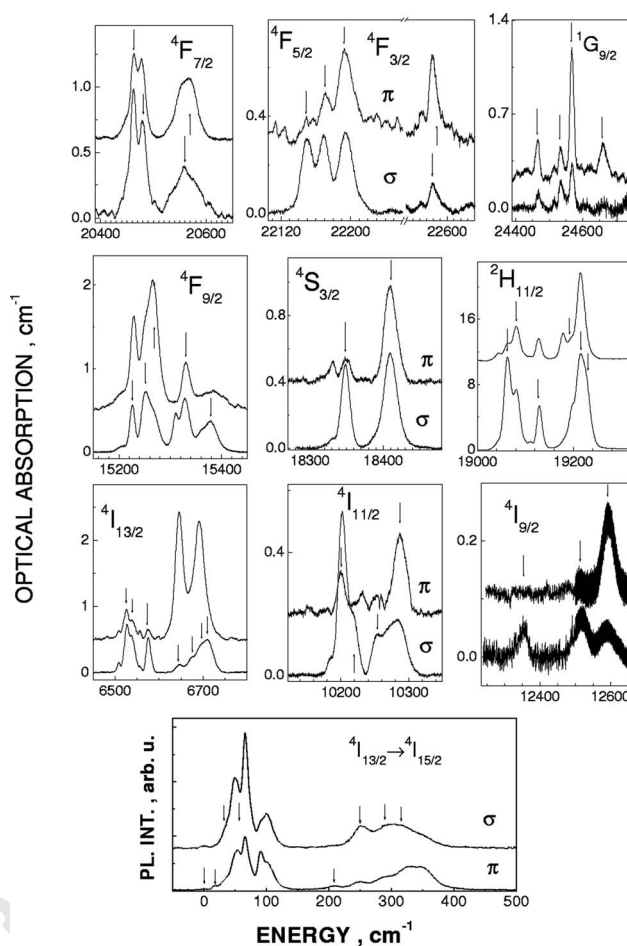


Fig. 4. PL of 10 K and OA of Er³⁺ in LBM crystal. [Er]=0.07 $\times 10^{20}$ cm⁻³. π -OA and σ -PL spectra appear arbitrarily displaced vertically.

The σ - and π -polarized PL and OA spectra clearly show differences as expected from the S_4 point symmetry of the 2b and 2d sites in the SG $I\bar{4}$. A good example of this situation are the ⁴I_{15/2}(0) \rightarrow ⁴S_{3/2} transitions. The possibility that the Er³⁺ low-temperature spectroscopic properties were determined by a monoclinic local symmetry, such as that described in NBM for $T < 241$ K, is ruled out by the presence of the well-defined polarization features shown in Fig. 4 and in previous works.⁷ In the monoclinic assumption, a unique $\Gamma_{3,4}$ irreducible representation IR for the 4f¹¹ Er³⁺ configuration would exist, with no differences between the σ and π -polarized spectra. Contrary to this, the Er³⁺ bands are seen either only in σ or simultaneously in σ and π configurations. Table 5 summarizes the energy of the levels determined, the experimental polarization of the observed ground-state transition (σ or $\sigma\pi$), and the corresponding experimental FWHM bandwidth. α -polarized spectra (not shown for brevity) were found to be very similar to σ -polarized ones; this shows that the observed transitions are dominated by electric dipole (ED) contributions.

In the absence of a magnetic field, the electric field of the lattice splits the ^{2S+1}L_J multiplets into $J + \frac{1}{2}$ Kramers doublets. The first step for the proper assignment of the observed levels to the IR ($\Gamma_{5,6}$ and $\Gamma_{7,8}$) of the S_4 point group is to determine the IR of the ground Stark level of

Table 5. Observed (E_o) at 10 K and Calculated for an Average S_4 Site (E_c) Energy Levels (cm^{-1}) of Er^{3+} in LBM Single Crystal^a

$2S+1L_J$	$\parallel RI$	E_o	E_c	ΔE_o	ΔE_c	$2S+1L_J$	$\parallel RI$	E_o	E_c	ΔE_o	ΔE_c
$^4I_{15/2}$	$\sigma \Gamma_{5,6}$	0	8	0	0	$^4S_{3/2}$	$\sigma \Gamma_{5,6}$	18,349	18,350	13	2
	$\sigma \pi \Gamma_{7,8}$	18	8	0	0		$(^2P_{3/2}) \sigma \pi \Gamma_{7,8}$	18,409	18,413	20	11
	$\Gamma_{5,6}$	33	41	5	5	$^2H_{11/2}$ $(^4G_{11/2})$	$\sigma \Gamma_{5,6}$	19,063	19,071	12	2
	$\Gamma_{7,8}$	54	58	3	3		$\sigma \pi \Gamma_{7,8}$	19,081	19,096	14	6
	$\Gamma_{7,8}$	208	209	4	4		$\sigma \pi \Gamma_{7,8}$	19,129	19,142	13	10
	$\Gamma_{7,8}$	251	242	7	7		$\sigma \Gamma_{5,6}$	19,199	19,192	7	7
	$\Gamma_{5,6}$	292	286	14	14		$\sigma \pi \Gamma_{7,8}$	19,215	19,204	18	8
	$\Gamma_{5,6}$	310	313	20	20		$\sigma \Gamma_{5,6}$	19,225	19,210	7	7
$^4I_{13/2}$	$\sigma \pi \Gamma_{7,8}$	6527	6524	6	3	$^4F_{7/2}$	$\sigma \pi \Gamma_{7,8}$	20,462	20,451	14	3
	$\sigma \Gamma_{5,6}$	6538	6524	9	3		$(^2G_{17/2}) \sigma \Gamma_{5,6}$	20,474	20,468	14	7
	$\sigma \Gamma_{5,6}$	6576	6574	9	4	$(^2G_{17/2})$	$\sigma \Gamma_{5,6}$	20,533	20,545	15	8
	$\sigma \pi \Gamma_{7,8}$	6646	6640	18	4		$\sigma \pi \Gamma_{7,8}$	20,566	20,567	28	15
	$\sigma \Gamma_{5,6}$	6675	6666	10	10		$\sigma \Gamma_{5,6}$	22,149	22,142	13	5
	$\sigma \pi \Gamma_{7,8}$	6691	6694	23	9	$(^2D_{15/2})$	$\sigma \Gamma_{5,6}$	22,170	22,158	13	3
	$\sigma \Gamma_{5,6}$	6710	6714	26	15		$\sigma \pi$	22,194	22,193	16	9
$^4I_{11/2}$ $(^2H_{11/2})$	$\sigma \pi \Gamma_{7,8}$	10,199	10,184	5	3	$^4F_{3/2}$	$\sigma \Gamma_{5,6}$	22,506	22,503	21	4
	$\sigma \Gamma_{5,6}$	10,202	10,194	7	5		$(^2D_{13/2}) \sigma \pi \Gamma_{7,8}$	22,547	22,549	28	12
	$\sigma \Gamma_{5,6}$	10,217	10,240	10	5	$^2G_{19/2}$ $(^4F_{9/2}, ^2H_{9/2})$	$\sigma \pi \Gamma_{7,8}$	24,466	24,450	14	3
	$\sigma \pi \Gamma_{7,8}$	10,232	10,260	10	6		$\sigma \Gamma_{5,6}$	24,534	24,544	15	1
	$\sigma \Gamma_{5,6}$	10,254	10,269	10	10		$\sigma \pi \Gamma_{7,8}$	24,567	24,568	15	10
	$\sigma \pi \Gamma_{7,8}$	10,286	10,282	18	11		$\sigma \pi \Gamma_{7,8}$	24,660	24,661	20	5
$^4I_{9/2}$	$\sigma \pi \Gamma_{7,8}$	12,352	12,342	11	3	$^4F_{9/2}$ $(^4I_{9/2})$	σ	—	12,448	1	1
	σ	—	12,448	1	1		σ	—	12,483	13	13
	σ	—	12,483	13	13		$\sigma \pi \Gamma_{7,8}$	12,518	12,504	20	3
	$\sigma \pi \Gamma_{7,8}$	12,518	12,504	20	3		$\sigma \pi \Gamma_{7,8}$	12,594	12,598	17	13
	$\sigma \pi \Gamma_{7,8}$	12,594	12,598	17	13		$\sigma \pi \Gamma_{7,8}$	15,226	15,227	13	1
$^4F_{9/2}$ $(^4I_{9/2})$	$\sigma \pi \Gamma_{7,8}$	15,226	15,227	13	1		$\sigma \Gamma_{5,6}$	15,252	15,263	13	10
	$\sigma \Gamma_{5,6}$	15,252	15,263	13	10		$\sigma \pi \Gamma_{7,8}$	15,266	15,267	18	1
	$\sigma \pi \Gamma_{7,8}$	15,266	15,267	18	1		$\sigma \pi \Gamma_{7,8}$	15,328	15,336	16	8
	$\sigma \pi \Gamma_{7,8}$	15,328	15,336	16	8		$\sigma \Gamma_{5,6}$	15,379	15,392	22	13
	$\sigma \Gamma_{5,6}$	15,379	15,392	22	13						

^a \parallel and IR indicate the OA observed polarization character and corresponding irreducible representation of the transition, respectively. ΔE_o is the observed OA FWHM line-width. ΔE_c is the energy separation simulated using SOM CF parameters (Ref. 28) for the nonequivalent $2b$ and $2d$ sites in the host.

the $^4I_{15/2}$ multiplet. The simplest case to analyze is the splitting of $J=5/2$ manifold. The $^4F_{5/2}$ manifold splits in two $\Gamma_{5,6}$ levels and one $\Gamma_{7,8}$ level. The experimental results in Fig. 4 show that the level with lowest energy in this multiplet has clearly a σ character, whereas the highest one is observed in σ and π configurations. The level in the middle seems to be mainly σ polarized, however this assignment is not free of uncertainty. To reach an unambiguous conclusion, we have performed the CF simulation described later in this section assuming either $\Gamma_{5,6}$ or $\Gamma_{7,8}$ IR for the ground Stark level. The assumption of a $\Gamma_{7,8}$ IR leads to an energy sequence for the $^4S_{3/2}$ multiplet in direct conflict with the polarization characters found experimentally. Therefore, the only possibility consistent with the experimental results is the assumption of $\Gamma_{5,6}$ IR for the ground Stark level of $^4I_{15/2}$ and a mainly σ character for the experimental spectra of the middle level of $^4F_{5/2}$.

The CF simulation has been performed in a way similar to that described previously for Er^{3+} in NBW and NBM crystals.⁷ The free ion (FI) and S_4 CF interactions

have been treated simultaneously through very complete H_{FI} and H_{S_4} Hamiltonians (see Ref. 7) with up to 20 and 6 in FI and CF parameters, respectively, using the entire basis set of wave functions. The initial values for the FI and CF parameters were those obtained for Er^{3+} in NBW. Table 6 summarizes the phenomenological FI and CF parameters resulting of the best simulation of the experimental sequence of energy levels.

3. Er^{3+} Radiative Processes

A recent work⁵ described the radiative processes of Er^{3+} in NBW through the application of the Judd–Ofelt (JO) formalism.^{22,23} Unfortunately, the polarized character of the Er^{3+} transitions in this latter crystal was ignored, and therefore the reported integrated absorption cross sections are uncertain. In this section, we shall revise the JO analysis of Er^{3+} in NBW taking into account the uniaxial character of the crystal, and we shall compare this with those also performed here for Er^{3+} in the NBM and LBM crystals.

Table 6. Phenomenological FI and CF Parameters (cm⁻¹) for Er³⁺ in LBM Single Crystal^a

Parameter	Value	Value in 2b	Value in 2d
E^0	35,003(1)		
E^1	6538.3(8)		
E^2	32.45(3)		
E^3	664.96(8)		
α	8.97(9)		
β	[-536]		
γ	[1790]		
ζ	2357.1(9)		
M^0 ^b	[5.9]		
P^2 ^c	[825]		
T^2	[400]		
T^3	[32]		
T^4	[238]		
T^6	[-289]		
T^7	[336]		
T^8	[299]		
B_0^2	412	470	401
B_0^4	-610(56)	-580	-564
B_4^4	$\pm 929(28)$	± 730	± 715
B_0^6	-170(35)	-85	-30
B_4^6	$\pm 460(20)$	± 576	± 556
S_4^6	$\pm 113(59)$	± 123	± 110
S_2 ^d	184	210	179
S_4	483	395	386
S_6	192	232	226
S_T	318	291	277
L	50		
σ^e	11.3		
Residue	4939.3		

^aItalic values are CF parameters calculated using the SOM model (Ref. 28) with previously determined 2b and 2d crystal data ($\rho=0.08$; effective charge for O=-0.8). Values in parentheses refer to estimate standard deviations in the indicated parameter. Values in square brackets were not allowed to freely vary in the parameter fitting.

$$^b M^2=0.56M^0; M^4=0.32M^0.$$

$$^c P^4=0.75P^2; P^6=0.50P^2.$$

^dThe CF strength parameter S_k and ST are defined as $S_T=[(1/3)\Sigma_k S_k^2]^{1/2}$, $S_k=\{1/(2k+1)[(B_0^k)^2+2\Sigma_q(B_q^k)^2+(S_q^k)^2]\}^{1/2}$.

^e■■■■■■■■

To apply the JO theory, the 300 K polarized OA spectra of Er³⁺ in NBW ([Er]_{crystal}=0.92×10²⁰ cm⁻³), NBM ([Er]_{crystal}=1.05×10²⁰ cm⁻³), and LBM ([Er]_{crystal}=0.56×10²⁰ cm⁻³) have been recorded. Table 7 shows the integrated absorption cross sections, $\Gamma_{JJ'}/[\text{Er}]$, for σ and π spectra. These experimental results have been averaged as $(2\sigma+\pi)/3$ and used to achieve the experimental oscillator strengths for each excited multiplet as

$$f_{\text{exp}} = \frac{4\epsilon_0 mc^2 \Gamma_{JJ'}}{e^2 \lambda^2 |\text{Er}|}. \quad (2)$$

The experimental average oscillator strengths obtained by us for Er³⁺ in NBW are larger than those reported in a previous work for the same NBW host.⁵ This is most likely due to the different conditions used for the experimental determination, in our case, explicitly taking into account the polarized character of the OA.

The JO theory has been described in a large number of works, and details of the treatment can be found elsewhere.^{22–24} We shall just mention that the ED oscillator strengths can be obtained as

$$f_{\text{ED,cal}} = \chi \frac{8\pi^2 mc}{3h\lambda(2J+1)} S_{JJ'}, \quad (3)$$

$$S_{JJ'} = \sum_{k=2,4,6} \Omega_k |\langle 4f^n[L,S]J \| U^k \| 4f^n[L',S']J' \rangle|^2, \quad (4)$$

where Ω_k are the JO parameters to be obtained from the minimization of the $f_{\text{exp}}-f_{\text{cal}}$ differences. Table 7 includes the Ω_k sets obtained for Er³⁺ in the Bi-based DT or DM considered here. In this calculation, we have used the $\langle \| U^k \| \rangle$ matrix elements provided previously²⁵ and the proper refractive indices for NBW and NBM¹⁰ and LBM (this work, Subsection 3.D.1). Also, magnetic dipole (MD) contributions to the experimental oscillator strengths have been taken into account to calculate the ED f_{exp} . Expressions for these contributions can be found elsewhere.²⁴

The Ω_k sets obtained for Er³⁺ in the three hosts are rather similar. This could be anticipated from the similar experimental values of the oscillator strengths. The Ω_k set corresponding to Er³⁺ in NBW is slightly larger than in the molybdates. However, in the three cases the ratios Ω_2/Ω_6 and Ω_4/Ω_6 fall in the 8.1–9.4 and 0.75–1.25 ranges, respectively. Using the calculated Ω_k sets, the radiative rates, $A_{JJ'}$, were obtained as described in the literature²⁵ and from them the branching ratios, $\beta_{JJ'}=A_{JJ'}/\Sigma_J A_{JJ'}$, and the radiative lifetimes, $\tau_r=1/\Sigma_J A_{JJ'}$, of the luminescence were calculated. Table 8 shows relevant results obtained for Er³⁺ in the NBM single crystal as a representative of the three compounds considered. Although the full set of multiplets was used in the calculations, Table 8 shows only transitions with $\beta > 4\%$.

Figure 5 shows an overview of relevant facts of the Er³⁺ PL emissions observed at 10 and 300 K in NBM. Although not shown for the sake of brevity, similar results were obtained for NBW and LBM single crystals. It is worth noting that the polarized character of the $^4I_{13/2} \rightarrow ^4I_{15/2}$ emission of interest for lasing, particularly the band at about 1520 nm, is more intense in π configuration. The nonpolarized spectral distribution reported previously in NBW:Er (Ref. 5) is intermediate between the now-resolved σ and π PL spectra.

To evaluate the laser efficiency of Er³⁺ in these hosts we have determined the experimental lifetimes of the $^4S_{3/2}$ and $^4I_{13/2}$ multiplets in the most diluted samples available. The experimental lifetime of the $^4S_{3/2}$ multiplet was excited resonantly at $\lambda=542$ nm and recorded at $\lambda_{\text{EMI}}(^4S_{3/2} \rightarrow ^4I_{15/2}) \approx 552$ nm. A single exponential was observed for all hosts and temperatures. The value was 20 μs at 300 K and 22 μs at 7 K. The $^4S_{3/2}$ experimental lifetime obtained is very short in comparison to the radiative value $\tau_r \approx 267$ μs calculated from the JO treatment; see Table 8. This short lifetime must be attributed to the interaction with the higher close-lying $^2H_{11/2}$ level with $\tau_r \approx 29$ μs . In fact, the thermal intensity evolution of the PL at $\lambda=520$ to 560 nm, see Fig. 5, shows the strong interaction at RT between the $^2H_{11/2}$ and $^4S_{3/2}$ multiplets.

AQ:
#11

Table 7. Average Wavelength, $\bar{\lambda}$, Integrated OA Cross Section, $\Gamma[\text{Er}]$, Experimental ED Oscillator Strength, $f_{\text{DE,exp}}$, Averaged ED Oscillator Strength, $f_{\text{DE,exp}}$, and Calculated ED Oscillator Strength, $f_{\text{DE,cal}}$, for $2s+1L_p$ Multiplets of Er^{3+} in NBW, NBM, LBM.^a

$^4I_{15/2} \rightarrow$	$\bar{\lambda}$ (nm)	NBW:Er			NBM:Er			LBM:Er		
		$\Gamma_{\sigma}/[\text{Er}]$ (10^{-27} cm^3)	$f_{\text{DE,exp}}$ ($\times 10^8$)	$f_{\text{DE,cal}}$ ($\times 10^8$)	$\Gamma_{\sigma}/[\text{Er}]$ (10^{-27} cm^3)	$f_{\text{DE,exp}}$ ($\times 10^8$)	$f_{\text{DE,cal}}$ ($\times 10^8$)	$\Gamma_{\sigma}/[\text{Er}]$ (10^{-27} cm^3)	$f_{\text{DE,exp}}$ ($\times 10^8$)	$f_{\text{DE,cal}}$ ($\times 10^8$)
$^4I_{15/2} \rightarrow$										
$^4G_{9/2}$	365	1.3	173	154			168			222
$^4G_{11/2}$	380	55	3861	3683			4340			4394
$H_{9/2}$	407	0.6	59	96			94			95
$F_{5/2,3/2}$	451	0.8	70	121	1.0	2.0	113	1	69	110
$F_{7/2}$	490	3.6	196	229	2.3	4.1	214	2.6	151	224
$H_{11/2}$	522	40	1673	1812	49	41	1922	45	1866	1865
$S_{3/2}$	547	1.4	63	60	0.9	2	54	0.9	43	52
$F_{9/2}$	660	6	190	191	6.1	9.4	177	7.2	220	211
$I_{9/2}$	800	1.0	32	25	1.5	2.5	24	2	43	34
$I_{11/2}$	980	2.8	46	89	4.5	7.1	63	3.4	79	49
$I_{13/2}$	1520	24	160 ^b	144	23	42	144 ^b	21	139 ^b	123
$\text{rms}(\Delta f)$				1.3			0.40			0.42
Ω_k (10^{-20} cm^2)			$\Omega_2=7.57, \Omega_4=0.71, \Omega_6=0.93$			$\Omega_2=7.37, \Omega_4=0.64, \Omega_6=0.78$			$\Omega_2=6.57, \Omega_4=0.87, \Omega_6=0.70$	

^aThe fit quality obtained with the Ω_k JO parameter sets is described by $\text{rms}(\Delta f)$.

^bMagnetic dipole contributions, f_{DM} , were evaluated and discounted as follows. NBW ($\|\sigma 0.68 \times 10^{-6}$ and $\|\sigma 0.66 \times 10^{-6}$), NBIM ($\|\sigma 0.70 \times 10^{-6}$ and $\|\sigma 0.68 \times 10^{-6}$), LBM ($\|\sigma 0.72 \times 10^{-6}$ and $\|\sigma 0.70 \times 10^{-6}$).

Table 8. ED and Magnetic Dipole (MD) Transition Probabilities, A_{ED} and A_{MD} ; Branching Ratios, β ; Radiative, τ_r , and Experimental, τ_{exp} , Lifetimes of Er^{3+} in NBM Calculated from the $\Omega_2=7.37$, $\Omega_4=0.64$, $\Omega_6=0.78$ Set^a

Transition	λ (nm)	$A_{\text{ED}}+A_{\text{MD}}$ (s ⁻¹)	β_{ij} (%)	τ_r (τ_{exp}) (μs)
$^4G_{9/2} \rightarrow ^4I_{13/2}$	481	84,906	81.84	9.6
$^4I_{15/2}$	367	9881	9.52	
$^4G_{11/2} \rightarrow ^4I_{15/2}$	382	179,592	93.81	5.2
$^2H_{9/2} \rightarrow ^4I_{11/2}$	698	1088	11.24	103
$^4I_{13/2}$	557	4491	46.41	
$^4I_{15/2}$	410	3757	38.83	
$^4F_{3/2} \rightarrow ^4I_{9/2}$	993	408	7.00	171
$^4I_{11/2}$	813	1745	29.92	
$^4I_{13/2}$	628	256	4.38	
$^4I_{15/2}$	447	3358	57.58	
$^4F_{5/2} \rightarrow ^4I_{13/2}$	643	2219	34.03	1.53
$^4I_{15/2}$	454	3689	56.57	
$^4F_{7/2} \rightarrow ^4I_{11/2}$	973	335	4.39	124
$^4I_{13/2}$	719	650	8.03	
$^4I_{15/2}$	491	6755	83.45	
$^2H_{11/2} \rightarrow ^4I_{15/2}$	527	33,322	97.15	29
$^4S_{3/2} \rightarrow ^4I_{13/2}$	850	927	24.77	267 (20 ^b)
$^4I_{15/2}$	549	2643	70.65	
$^4F_{9/2} \rightarrow ^4I_{11/2}$	1976	153	5.96	389
$^4I_{13/2}$	1151	130	5.06	
$^4I_{15/2}$	660	2273	88.39	
$^4I_{9/2} \rightarrow ^4I_{13/2}$	1709	88	33.03	3737
$^4I_{15/2}$	812	173	64.54	
$^4I_{11/2} \rightarrow ^4I_{13/2}$	2758	36+14	87.88	2415 (116 ^b)
$^4I_{15/2}$	991	364	12.12	
$^4I_{13/2} \rightarrow ^4I_{15/2}$	1547		100	
NBW [Er]= 2×10^{18} cm ⁻³		213+94	3254	(2400 ^b)
NBM [Er]= 7.5×10^{19} cm ⁻³		204+108	3200	(2300 ^b)
LBM [Er]= 7×10^{18} cm ⁻³		211+117	3048	(2060 ^b)

^aOnly transitions with $\beta > 4\%$ are shown.

^b300 K experimental ⁴S_{3/2}, ⁴I_{11/2}, and ⁴I_{13/2} lifetimes of Er in NBM crystals doped with the lowest concentration available ⁴I_{13/2} experimental lifetimes of Er in NBW and LBM are also included.

For ${}^4I_{13/2}$ lifetime determination, the 300 K PL was excited at $\lambda_{\text{exc}}({}^4I_{15/2} \rightarrow {}^4I_{11/2}) \approx 980$ nm and measured at $\lambda_{\text{EMI}}({}^4I_{13/2} \rightarrow {}^4I_{15/2}) \approx 1540$ nm using the lowest concentration available for each host. The results are included in Table 8. This excitation scheme should produce realistic measurement in view of the short experimental lifetime reported for the ${}^4I_{11/2}$ multiplet, namely, $\tau = 116 \mu\text{s}$.⁶ Moreover, the emission reabsorption (${}^4I_{15/2} \rightarrow {}^4I_{13/2}$) leading to artificial delay enlargement of the intensity decay, is negligible owing to the very low absorption of the samples used.

4. DISCUSSION

The laser efficiency of a $2S+1L_J$ multiplet is related to the branching ratio distribution, emission cross section σ_{EMI} , and quantum efficiency η , among other parameters.

For a given transition, the absolute value of σ_{emi} can be estimated by the reciprocity principle²⁶ as

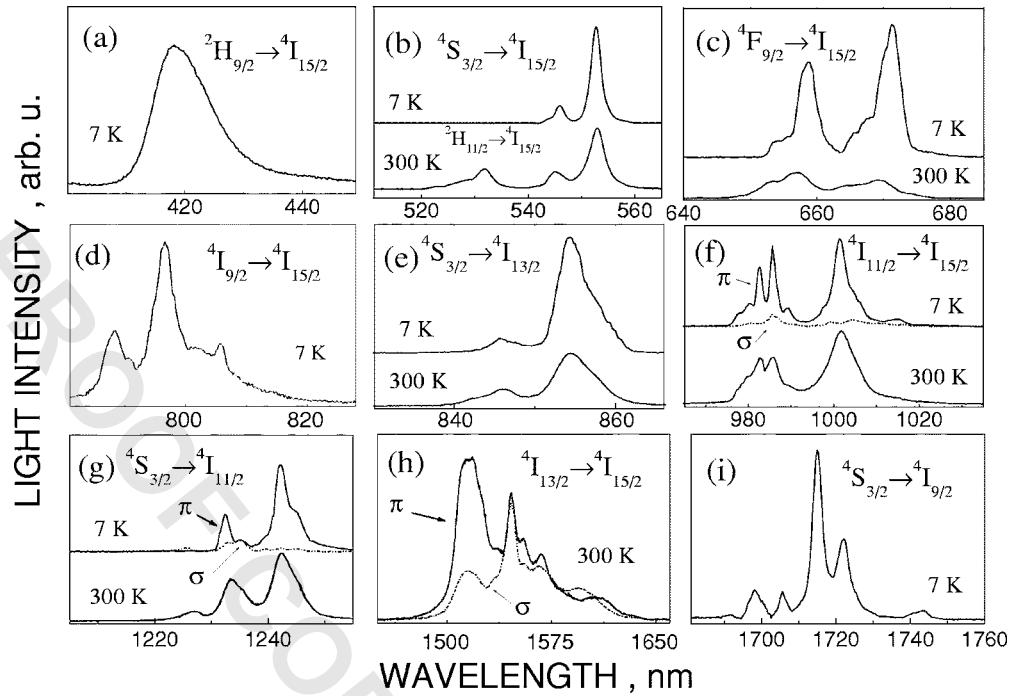


Fig. 5. Er³⁺ PL in NBM.

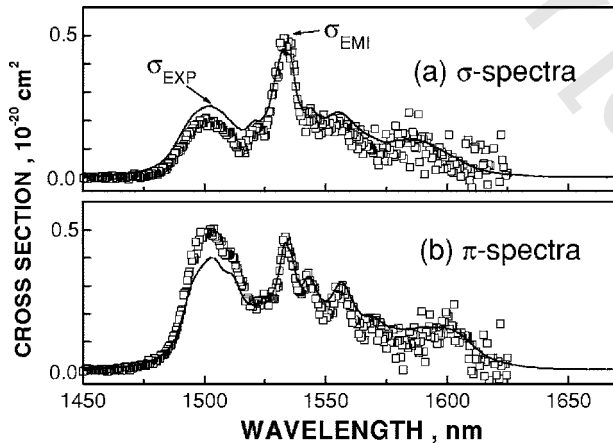


Fig. 6. Comparison between the experimental PL spectral distribution (σ_{EXP} , line) and calculated $^4I_{13/2} \rightarrow ^4I_{15/2}$ emission cross section (σ_{EMI} , points) of Er³⁺ in NBW single crystal. (a) σ -polarized spectra. (b) π -polarized spectra.

$$\sigma_{\text{EMI}} = \sigma_{\text{GSA}} \frac{Z_l}{Z_u} e^{(E_{zl} - h\nu)/k_B T}, \quad (5)$$

APC: where $\sigma_{\text{GSA}} = \alpha_{\text{GSA}}/[\text{Er}]$ is the GSA cross section; Z_u and Z_l are the partition functions of the upper and lower multiplets, respectively; and E_{zl} is the energy difference between the lowest Stark levels of both multiplets. Z_u , Z_l , and E_{zl} , can be obtained from previous results for NBW and NBM⁷ and from those reported in Table 5 for LBM. In all the hosts considered here, $Z_l/Z_u \approx 1$ was found for the $^4I_{13/2} \rightarrow ^4I_{15/2}$ laser channel.

Figure 6 shows the experimental spectral dependence of the 300 K $^4I_{13/2} \rightarrow ^4I_{15/2}$ Er³⁺ emission in NBW after normalization to the absolute peak value calculated obtained by using Eq. (4). Within the experimental uncer-

tainty, Er-doped NBM and LBM have similar spectral shapes and peak values similar to those shown in Fig. 6 for Er-doped NBW. At $\lambda = 1535$ nm, the peak emission cross sections in both polarization configurations are similar, $\sigma_{\text{EMI}} \approx 0.5 \times 10^{-20} \text{ cm}^2$, but in general, σ_{EMI} is slightly larger in π configuration, particularly for $\lambda \approx 1500$ nm.

The Er peak σ_{emi} value around 1530–1550 nm in NBW can be compared to those of Er in YAG.²⁷ For this standard laser crystal, a peak 300 K σ_{EMI} ($\lambda \approx 1530$ nm) $\approx 0.7 \times 10^{-20} \text{ cm}^2$ has been found, but laser action takes place for $\sigma_{\text{EMI}} \geq 0.2 \times 10^{-20} \text{ cm}^2$. This shows that the cross sections of Er³⁺ in XBi(YO₄)₂ crystals are of the magnitude required for laser operation. The expected spectral laser tunability of Er in NBW can be estimated from the effective emission cross-section σ_{EFF} ,

$$\sigma_{\text{EFF}} = \beta \sigma_{\text{EMI}} - (1 - \beta) \sigma_{\text{GSA}}, \quad (6)$$

where β is the inversion coefficient. To achieve laser oscillation $\sigma_{\text{eff}} > 0$ is required. Figure 7 shows that a moderate inversion coefficient ($\beta \geq 0.3$) is needed to achieve the threshold laser condition. For a medium value of the inversion coefficient $\beta = 0.5$, the spectral range of tunability calculated is up to approximately 88 nm with a FWHM of approximately 60 nm. This bandwidth would allow mode-locked laser pulses of 50 fs for Gaussian pulse shape or 70 fs for sech² pulse shape.

The $^4I_{13/2}$ quantum efficiencies $\eta = \tau_{\text{exp}}/\tau_r$ obtained for the disordered DT and DM hosts considered here are $\eta \approx 0.68$ to 0.74. A more efficient $\eta = 0.84$ value has been reported for Er in NBW.⁵ In our view, this latter result is overestimated owing to the recording conditions of the $\tau_{\text{exp}} \approx 4750 \mu\text{s}$ lifetime, i.e., pumping the $^4S_{3/2}$ multiplet and detecting with cooled Ge photodiode. Moreover, the radiative lifetime previously calculated⁵ is uncertain because the MD contribution to the $^4I_{13/2} \rightarrow ^4I_{15/2}$ transition

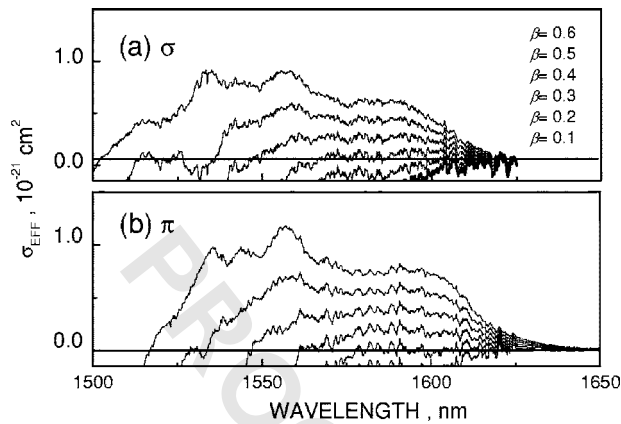


Fig. 7. Spectral dependence of the effective emission cross section of Er in NBW.

probability was ignored. Another determination of the $^4I_{13/2}$ Er^{3+} experimental lifetime in NBW reported $\tau_{\text{exp}} \approx 3400 \mu\text{s}$,⁶ is that this is closer to the τ_{exp} values obtained in this work. Although detailed information of the characteristics of the previously used detectors is not available, the larger lifetime values previously reported are likely due to detector rise-time limitations or to emission reabsorption. In our case, all these artifacts are excluded among to the fast detector rise time (3 ns) and very low Er concentration ($[\text{Er}] \approx 10^{18} \text{ cm}^{-3}$) used, which also excludes a lifetime reduction by energy transfer between Er–Er neighbors.

In view of the σ_{eff} and η values achieved here, laser emission at $1.5 \mu\text{m}$ in Er-doped NBW, NBM, and LBM crystals seems feasible. The broad bandwidths of these crystals allow an efficient absorption of the radiation pumping even using laser diodes not specifically wavelength matched and as mentioned above a broad laser tunability range can be expected. To optimize these applications, the physical contributions to the optical linewidth must be identified. In Subsection 3.C, it was shown that LBM is isostructural to NBW and NBM, and all of them can be described with the symmetry of the SG $I\bar{4}$ with two different lattice sites for Er^{3+} , thus we refer to this fact as a *site contribution* to the bandwidth. The transformation upon cooling of the SG $I\bar{4}_1/a$ to the SG $I\bar{4}$ cannot be justified on the basis of an off-stoichiometry crystal composition, rather it seems likely that the thermal history of the crystal plays a major role. Moreover, since the $2b$ and $2d$ sites are shared by the alkaline, Bi^{3+} and Er^{3+} cations, multiple environments around Er^{3+} are associated to different cationic distributions, we refer to this fact as an *environment contribution* to the bandwidth. The purpose of the following discussion is to account for the influence of the first of these two contributions.

The Er^{3+} CF analysis made in Subsection 3.D.2 yielded the phenomenological FI and CF parameters of an average S_4 Er^{3+} center. The FI parameters are roughly the same for similar hosts, while individual sets of CF parameters in both $2b$ and $2d$ sites can be calculated through the simple overlap model²⁸ (SOM), by using established $\text{Bi(I)}\text{--O}$ and $\text{Bi(II)}\text{--O}$ crystallographic distances given in Table 5. Table 6 (SOM column) includes these two collec-

tions of semiempirical calculated CF parameters in the S_4 symmetry. Using each one of these CF parameter sets along with the common optimized FI parameters, separated sequences of energy levels have been derived for Er^{3+} in the two sites. The energy differences, ΔE_c , between these two sequences for each Stark level provides the *site contribution* to the bandwidth observed at low temperature.

Table 5 shows a comparison of the calculated ΔE_c *site contributions* and the experimental ΔE_o FWHM bandwidths for Er^{3+} in LBM. Results for NBW and NBM are similar and not shown for the sake of brevity. From this comparison, it can be observed that the *site contributions* are generally slightly lower than the experimental bandwidths, i.e., they are inside the experimental linewidths and not resolved under the experimental conditions used. This implies that the *environment contribution* can be roughly estimated as half of the experimental linewidth. This is still much larger than the inhomogeneous broadening observed in ordered DT or DM hosts. Figure 8 shows a comparison with monoclinic α -KGW where Er

APC:
#5

sits in a unique site and lattice disorder does not exist. Finally, it should be mentioned that although these hosts can be grown with very high Er concentration,²⁹ their disordered nature favors the presence of a fraction of Er–Er pairs that will introduce emission losses. Therefore the demonstration of laser action is a possible but challenging task that likely should balance absorption of pumping (likely by codoping with Yb in the diode pumped case) and Er concentration.

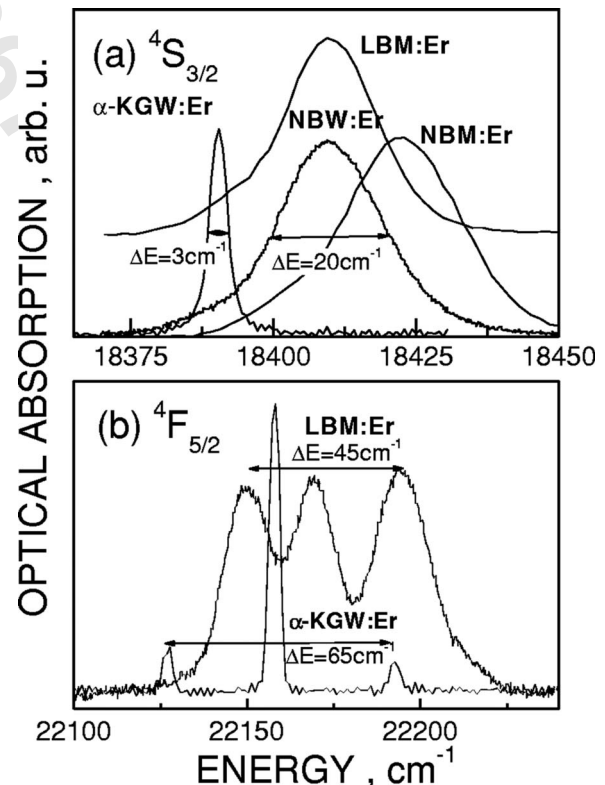


Fig. 8. Comparison of the low-temperature OA of Er^{3+} in “ordered” (α -KGW) and “disordered” DT and DM. (a) Bandwidths for a $^4S_{3/2}$ Stark level. (b) CF splitting of $^4F_{5/2}$ multiplet.

5. CONCLUSIONS

NBW, NBM, and LBM crystals used in this work are negative uniaxial isostructural crystalline hosts with the symmetry of the SG $I\bar{4}$. Even when doped with a significant concentration of Er [Er]_{melt} \approx 1 mol.%, the compounds have a congruent melting, and therefore they can be grown by the Cz method.

Er^{3+} is placed in two nonequivalent lattice sites of the hosts and experiences a distribution of CFs associated to the Li (or Na) and Bi random occupancy of these lattice sites. As a consequence of this crystallographic feature, the peak absorption and emission Er^{3+} cross sections are lower than in the ordered monoclinic DT laser hosts, but the balance between the $^4I_{13/2}$ emission and absorption cross sections is positive even at moderate inversion ratios $\beta \geq 0.4$, which suggests possible laser action at RT along with some degree of tunability.

The spectroscopic properties of Er in NBW, NBM, and LBM hosts are rather similar and show polarized features in accordance with the uniaxial character of the crystal lattices and with the S_4 local symmetry of the $2b$ and $2d$ sites of the tetragonal SG $I\bar{4}$. The polarized nature of the spectroscopy indicates that the Er^{3+} centers keep constant relative orientations and it excludes a monoclinic local symmetry. The energy difference for a given Er^{3+} level in the two lattice sites is lower than the experimental bandwidth; this difference was not experimentally resolved in the spectroscopic measurements performed in this work.

ACKNOWLEDGMENTS

The authors acknowledge the financial support through the Spanish projects MAT2002-04603-C05-05 and CAM MAT/0434/2004 and also from the European Commission, project DT-CRYS, UE NMP3-CT-2003-505580. The GRICE (Portugal)–CSIC (Spain) cooperation agreement is gratefully acknowledged. M. Rico is supported by the Education and Culture Ministry of Spain under Ramón y Cajal programme.

Corresponding author C. Cascales's e-mail address is ccascales@icmm.csic.es. Corresponding author C. Zaldo's e-mail address is cezaldo@icmm.csic.es.

REFERENCES

- M. Rico, J. Liu, U. Griebner, V. Petrov, M. D. Serrano, F. Esteban-Betegón, C. Cascales, and C. Zaldo, "Tunable laser operation of ytterbium in disordered single crystals of $\text{Yb}:\text{NaGd}(\text{WO}_4)_2$," *Opt. Express* **12**, 5362–5367 (2004).
- J. Liu, J. M. Cano-Torres, C. Cascales, F. Esteban-Betegón, M. D. Serrano, V. Volkov, C. Zaldo, M. Rico, U. Griebner, and V. Petrov, "Growth and continuous-wave laser operation of disordered crystals of $\text{Yb}^{3+}:\text{NaLa}(\text{WO}_4)_2$ and $\text{Yb}^{3+}:\text{NaLa}(\text{MoO}_4)_2$," *Phys. Status Solidi A* **202**, R29–R31 (2005).
- S. Rivier, M. Rico, U. Griebner, V. Petrov, M. D. Serrano, F. Esteban-Betegón, C. Cascales, C. Zaldo, M. Zorn, and M. Weyers, "Sub-80 fs pulses from a mode-locked $\text{Yb}:\text{NaGd}(\text{WO}_4)_2$ laser," in *Conference on Lasers and Electro-Optics/Europe, Munich, Germany, June 12–17, 2005*, CLEO/Europe-EQEC 2005 Conference Digest CD-ROM (2005), paper CF4-4-THU.
- A. A. Kaminski, *Crystalline Lasers* (CRC, 1996).
- D. K. Sardar, C. C. Russell III, R. M. Yow, J. B. Gruber, B. Zandi, and E. P. Kokanyan, "Spectroscopic analysis of the Er^{3+} ($4f^{11}$) absorption intensities in $\text{NaBi}(\text{WO}_4)_2$," *J. Appl. Phys.* **95**, 1180–1183 (2004).
- K. A. Subbotin, E. V. Zharikov, and V. A. Smirnov, "Yb and Er-doped single crystals of double tungstates $\text{NaGd}(\text{WO}_4)_2$, $\text{NaLa}(\text{WO}_4)_2$, and $\text{NaBi}(\text{WO}_4)_2$ as active media for lasers operating in the 1.0 and 1.5 μm ranges," *Opt. Spectrosc.* **92**, 601–608 (2002) [*Opt. Spektrosk.* **92**, 657–664 (2002)].
- M. Rico, V. Volkov, C. Cascales, and C. Zaldo, "Measurements and crystal field analysis of Er^{3+} energy levels in crystals of $\text{NaBi}(\text{MoO}_4)_2$ and $\text{NaBi}(\text{WO}_4)_2$ with local disorder," *Chem. Phys.* **279**, 73–86 (2002).
- International Tables for Crystallography* (Kynoch, 1974), Vol. 4.
- SHELXTL Version 6.10 software package, Siemens Energy and Automation Incorporated Analytical Instrumentation.
- V. Volkov, M. Rico, A. Méndez-Blas, and C. Zaldo, "Preparation and properties of disordered $\text{NaBi}(\text{XO}_4)_2$, $X = \text{W}$ or Mo , crystals doped with rare earths," *J. Phys. Chem.* **63**, 95–105 (2002).
- M. Luomajarvi, E. Rauhala, and M. Hautala, "Oxygen detection by non-Rutherford proton backscattering below 2.5 MeV," *Nucl. Instrum. Methods Phys. Res. B* **9**, 255–258 (1985).
- Y. Cassagnou, J. M. F. Jeronymo, G. S. Mani, A. Sadeghi, and P. D. Forsyth, "The $^7\text{Li}(p, \alpha)$ alpha reaction," *Nucl. Instrum. Methods* **33**, 449–457 (1962).
- D. Heck, "Three-dimensional lithium microanalysis by the $^7\text{Li}(p, \alpha)$," *Nucl. Instrum. Methods Phys. Res. B* **30**, 486–490 (1988).
- A. Sagara, K. Kamada, and S. Yamaguchi, "Depth profiling of lithium by use of the nuclear reaction $^7\text{Li}(p, \alpha)^4\text{He}$," *Nucl. Instrum. Methods Phys. Res. B* **34**, 465–469 (1988).
- G. Vizkelethy, "Simulation and evaluation of nuclear reaction spectra," *Nucl. Instrum. Methods Phys. Res. B* **45**, 1–5 (1990).
- J. Hanuza, M. Maczka, and J. H. van der Mass, "Polarized IR and Raman spectra of tetragonal $\text{NaBi}(\text{WO}_4)_2$, $\text{NaBi}(\text{MoO}_4)_2$ and $\text{LiBi}(\text{MoO}_4)_2$ single crystals with scheelite structure," *J. Mol. Struct.* **348**, 349–352 (1995).
- J. Hanuza, A. Haznar, M. Maczka, A. Pietraszko, A. Lemiec, J. H. van der Maas, and E. T. G. Lutz, "Structure and vibrational properties of tetragonal scheelite $\text{NaBi}(\text{MoO}_4)_2$," *J. Raman Spectrosc.* **28**, 953–963 (1997).
- M. Maczka, E. P. Kokanyan, and J. Hanuza, "Vibrational study and lattice dynamics of disordered $\text{NaBi}(\text{WO}_4)_2$," *J. Raman Spectrosc.* **36**, 33–38 (2005).
- A. Waskowska, L. Gerward, J. Staun Olsen, M. Maczka, T. Lis, A. Pietraszko, and W. Morgenroth, "Low-temperature and high-pressure structural behaviour of $\text{NaBi}(\text{MoO}_4)_2$ —an X-ray diffraction study," *J. Solid State Chem.* **178**, 2218–2224 (2005).
- P. V. Kletsov, V. A. Vinokurov, and R. F. Klevtsova, "Double molybdates and tungstates of alkali metals with bismuth, $\text{M}^+\text{Bi}(\text{TO}_4)_2$," *Z. Kristallogr.* **18**, 1192–1197 (1973).
- J. Liu, J. M. Cano-Torres, F. Esteban-Betegón, M. D. Serrano, C. Cascales, C. Zaldo, M. Rico, U. Griebner, and V. Petrov, "Continuous-wave diode-pumped operation of an $\text{Yb}:\text{NaLa}(\text{WO}_4)_2$ laser at room temperature," *Opt. Laser Technol.* (available online December 9, 2005).
- B. R. Judd, "Optical absorption intensities of rare-earth ions," *Phys. Rev.* **127**, 750–761 (1962).
- G. S. Ofelt, "Intensities of crystal spectra of rare-earth ions," *J. Chem. Phys.* **37**, 511–520 (1962).
- C. Görller-Walrand and K. Binnemans, "Spectral intensities of $f-f$ transitions," in *Handbook on the Physics and Chemistry of Rare Earths*, K. A. Gschneider, Jr. and L. Eyring, eds. (Elsevier Science, 1998), Vol. 25, p. 101.
- M. J. Weber, "Probabilities for radiative and nonradiative decay of Er^{3+} in LaF_3 ," *Phys. Rev.* **157**, 262–272 (1967).

APC:
#6APC:
#7APC:
#8

26. D. E. McCumber, "Einstein relations connecting broadband emission and absorption spectra," *Phys. Rev.* **136**, A954–A957 (1964).
27. J. Koetke and G. Huber, "Infrared excited-state absorption and stimulated emission cross sections of Er^{3+} doped crystals," *Appl. Phys. B* **61**, 151–158 (1995).
28. P. Porcher, M. Couto dos Santos, and O. Malta, "Relationship between phenomenological crystal field parameters and crystal structure. The simple overlap model," *Phys. Chem. Chem. Phys.* **1**, 397–405 (1999).
29. Z. Cheng, Q. Lu, S. Zhang, J. Liu, X- Yi, F. Song, Y. Kong, J. Han, and H. Chen, "Growth and properties of $\text{NaEr}(\text{WO}_4)_2$ crystals," *J. Cryst. Growth* **222**, 797–800 (2001).

PROOF COPY [66670] 502610JOB